Available online at www.sciencedirect.com
SCIENCE DIRECT®
Journal of Sound and Vibration 288 (2005) 195–213
JOURNAL OF SOUND AND VIBRATION
www.elsevier.com/locate/jsvi

Wave boundary element to study Lamb wave propagation in plates

Jing Jin[a], Ser Tong Quek[a,*], Quan Wang[b]

[a]*Department of Civil Engineering, National University of Singapore, 119260 Singapore*
[b]*Department of Mechanical, Materials & Aerospace Engineering, University of Central Florida, Orlando, FL 32816-2450, USA*

Received 28 May 2004; received in revised form 29 December 2004; accepted 4 January 2005
Available online 17 May 2005

Abstract

By using analytical mode shapes as the interpolating functions for both displacements and stresses on the reference edges of a plate, a wave element is formulated for use in the boundary element method to study Lamb wave propagation and interaction in plates, to achieve both accuracy and computational efficiency. Lamb wave interaction with a notch is investigated using this method. The results with respect to wave transmission, reflection and mode conversion are consistent with physical considerations of Lamb mode shape and energy conservation. It is shown through the reflection coefficients that S_0 Lamb wave is more sensitive than A_0 wave for detecting a shallow notch in a plate. These coefficients can be used to aid the characterization of the presence of a notch and contribute to quantitative non-destructive evaluation methodology for plate structures. Time history results are obtained by conducting Fourier transform on the coefficients solved in frequency domain. Comparison with experiment results shows the suitability of the method for wave propagation studies in relation to damage detection.

1. Introduction

The use of Lamb waves for non-destructive evaluation (NDE) of plates has attracted attention due to its interrogating efficiency over a reasonably extensive region. By sending a Lamb wave

*Corresponding author. Tel.: +65 68742263; fax: +65 68742248.
E-mail addresses: mpejingj@nus.edu.sg (J. Jin), cveqst@nus.edu.sg (S. Tong Quek).

0022-460X/$ - see front matter © 2005 Elsevier Ltd. All rights reserved.
doi:10.1016/j.jsv.2005.01.051

pulse, a structural discontinuity, if exists, can be located by interpreting reflected Lamb wave packages from the discontinuity. However, the presence of multi-mode and dispersion of Lamb waves complicate the extraction of useful information from the measured wave signals. Significant progress has been made by reducing the excited Lamb waves to single mode by using equipment such as wedge transducers [1], comb transducers [2] and inter-digital transducers [3–5]. However, most detection methods yield results that are qualitative in nature. Development of comprehensive and good quantitative methods invariably needs a good analytical or numerical model to study the effect of a whole spectrum of parameters which otherwise would not be feasible experimentally. Analytical solutions are almost impossible except for simple problems, and hence an efficient numerical program to model the complicated elastic wave interaction problem even for a single Lamb mode is essential.

A numerical method to discretize a whole plate can be very inefficient for wave propagation problems as the element size has to be small yet large enough to minimize numerical errors. Al-Nassar et al. [6] combined the finite element method (FEM) to simulate the localized plate region containing weldment and Lamb mode expansion to represent the wave field in the remaining region of the plate. A similar procedure was used by Chang [7] and Moulin et al. [8] to study the interaction of Lamb wave with defects and the excitation of Lamb wave by PZT patch, respectively. In both cases, only a region of the plate containing structural discontinuities is meshed with finite elements, while the known analytical wave propagation solution is applied on the remaining portion of the plate. The significantly reduced computation effort made the solution possible.

In NDE experiments to detect defects, only that portion of waves that have not been complicated by interactions resulting from incident and multiply-reflected waves is of interest. Hence, a numerical model to capture localized effects rather than the global behavior is adequate. As with experiments, the wave interaction can be evaluated by measuring the amplitudes of the reflected and transmitted Lamb modes at two selected boundaries of the plate under investigation. Thus, only the segment of the plate within the selected boundaries needs to be modeled if Lamb waves pulses are used, which is the case in some NDE techniques. Cho and Rose [9] developed the hybrid boundary element method (BEM) to monitor a segment of plate by forcing the mode shape of Lamb waves on the two reference imaginary edges to obtain the relationship between displacement and stress for the case without wave reflections. The amplitudes of each Lamb modes passing through the reference edges are subsequently computed. The ratio of the amplitudes can then be compared with experimentally measured values, facilitating the development of NDE on plates to a quantitative level [10,11]. In their model, the imaginary edges are discretized and numerically integrated by the standard BEM procedure. The use of higher-order interpolating function to reduce the number of elements required can be problematic. This is because the Lamb mode shape values are forced on each discrete node of the edges rather than through the entire length of the edge. The interpolating function and the Lamb mode shape are not the same and the resulting actual mode shape implied in the numerical integration is distorted. Hence, the meshes on the boundaries need to be rather fine to achieve reasonably accurate results.

The objective of this paper is to present a wave element that allows for a coarser element to be used in BEM to model wave propagation and interaction within a localized segment of a plate containing a discontinuity. Conceptually, this entails using the exact mode shape function and

integrating each of the two imaginary edges as one single element, termed herein as the wave element. Experimental results of Lamb wave interaction in a plate with and without a notch are used to validate the model in terms of both the reflection coefficients and time history response as well locate the notch position as in NDE. The computational accuracy and efficiency will be demonstrated.

2. BEM formulation for steady-state Lamb wave propagation

2.1. BEM for steady-state elasto-dynamics

Lamb waves are fundamentally plane strain waves [12]. For the 2D elasto-dynamics problem, the basic BEM integral equation without body force is [13]

$$c^i \vec{u}^i + \int_\Gamma \vec{T}^* \vec{u}\, \mathrm{d}\Gamma = \int_\Gamma \vec{u}^* \vec{T}\, \mathrm{d}\Gamma, \tag{1}$$

where $\vec{u}^i$ denotes the 2×1 vector of displacements at the boundary point i where the load is applied, c^i is a 2×2 array of constants and Γ is the boundary. The fundamental solutions, $\vec{u}^*$ and $\vec{T}^*$, are given by

$$\vec{u}^* = \begin{bmatrix} u^*_{11} & u^*_{12} \\ u^*_{21} & u^*_{22} \end{bmatrix}, \quad \vec{T}^* = \begin{bmatrix} T^*_{11} & T^*_{12} \\ T^*_{21} & T^*_{22} \end{bmatrix}, \tag{2}$$

$$u^*_{lk} = \frac{1}{2\pi\rho C_s^2} [\psi \delta_{lk} - \chi r_{,l} r_{,k}], \tag{3}$$

$$T^*_{lk} = \frac{1}{2\pi} \left\{ \left(\frac{\mathrm{d}\psi}{\mathrm{d}r} - \frac{1}{r}\chi \right) \left(\delta_{kl} \frac{\partial r}{\partial n} + r_{,k} n_l \right) - \frac{2}{r}\chi \left(n_k r_{,l} - 2 r_{,k} r_{,l} \frac{\partial r}{\partial n} \right) - 2 \frac{\mathrm{d}\chi}{\mathrm{d}r} r_{,k} r_{,l} \frac{\partial r}{\partial n} + \left(\frac{C_p^2}{C_s^2} - 2 \right) \left(\frac{\mathrm{d}\psi}{\mathrm{d}r} - \frac{\mathrm{d}\chi}{\mathrm{d}r} - \frac{\chi}{r} \right) r_{,l} n_k \right\}, \tag{4}$$

where l and k range from 1 to 2, δ_{lk} is the Kronecker delta function, ρ the density, C_s and C_p the compression and shear wave velocities, respectively, r the distance between the load point (which is used to form the set of equations to be solved, often known as the collecting point) and the field point and n the unit normal to the surface. ψ and χ are given by

$$\psi = K_0 \left(\frac{\mathrm{i}\omega r}{C_s} \right) + \frac{C_s}{\mathrm{i}\omega r} \left[K_1 \left(\frac{\mathrm{i}\omega r}{C_s} \right) - \frac{C_s}{C_p} K_1 \left(\frac{\mathrm{i}\omega r}{C_p} \right) \right], \tag{5a}$$

$$\chi = K_2 \left(\frac{\mathrm{i}\omega r}{C_s} \right) - \frac{C_s^2}{C_p^2} K_2 \left(\frac{\mathrm{i}\omega r}{C_p} \right) \tag{5b}$$

in which ω is the angular frequency and K_0, K_1, and K_2 are the modified zero-, first- and second-order Bessel functions of the second kind, respectively.

By discretizing the boundary Γ, Eq. (1) can be approximated as

$$c^i\vec{u}^i + \sum_j \hat{H}^{ij}\vec{u}^j = \sum_j G^{ij}\vec{T}^j, \tag{6}$$

where

$$\hat{H}^{ij} = \int_{\Gamma_j} \vec{T}^* \, d\Gamma_j, \quad G^{ij} = \int_{\Gamma_j} \vec{u}^* \, d\Gamma_j \quad \text{and} \quad j = 1, 2, \ldots,$$

number of boundary elements.

The diagonal terms ($i = j$), $\hat{H}^{ii}$ and G^{ii}, pose computational difficulties due to singularities in the Bessel functions at $r = 0$. By expanding the Bessel functions, G^{ii} can be expressed as a sum of a non-singular part, fn, and a logarithmic part, $A\log(r)$, which can be approximated by a logarithmic quadrature integration scheme, while $\hat{H}^{ii}$ can also be expressed as a sum of a non-singular term, fn^d, and a singular term, fs. The singular term is the same as that for the elasto-static problem. Denoting the elasto-static equivalent terms as $(\hat{H}^{ii})^s = fn^s + fs$, where fn^s is the non-singular term, the LHS diagonal terms can be expressed as

$$c^i + \hat{H}^{ii} = c_i + fs + fn^d = c^i + (\hat{H}^{ii})^s + fn^d - fn^s. \tag{7}$$

As in the elasto-static problem, the singular part, $c^i + (\hat{H}^{ii})^s$ can be obtained by considering rigid-body motion without having to perform integration [13]. Therefore, singularity is circumvented in Eq. (7), and a steady-state elasto-dynamics problem can be solved by using Eq. (6), which can be written in a more compact form as

$$\sum_j H^{ij}\vec{u}^j = \sum_j G^{ij}\vec{T}^j, \tag{8}$$

where

$$H^{ij} = \begin{cases} c^i + \hat{H}^{ii}, & i = j, \\ \hat{H}^{ij}, & i \neq j. \end{cases}$$

2.2. Hybrid BEM for Lamb wave propagation

For practical reasons, the domain of interest in the application of Lamb wave propagation for NDE is confined to a small area. For example, in a 2D plate, the region is bounded by two traction-free boundaries, Γ^{Top} and Γ^{Bot}, and two imaginary edges, Γ^+ and Γ^-, as shown in Fig. 1. For a uniform segment, incident Lamb mode propagates into the domain from the left edge, and out of the domain at the right edge without mode conversion and virtually no decay. If some structural discontinuity (such as a notch) exists in the domain, the incident Lamb mode partially converts into other modes, and all these modes may interact and propagate out of the domain in either direction. Therefore, the acoustic field at the edges can be

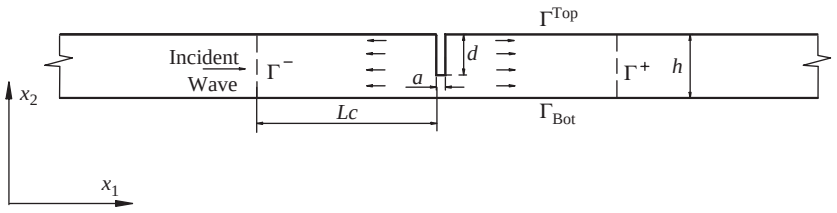

Fig. 1. 2D model of a plate segment with a notch.

expressed as [11]

$$\vec{u} = \begin{cases} A_p^I \vec{\bar{u}}_p^I \, \mathrm{e}^{\mathrm{i}k_p x_1} + \sum\limits_n A_n^- \vec{\bar{u}}_n^- \, \mathrm{e}^{-\mathrm{i}k_n x_1} & (x_1 \subset \Gamma^-), \\ \sum\limits_n A_n^+ \vec{\bar{u}}_n^+ \, \mathrm{e}^{\mathrm{i}k_n x_1} & (x_1 \subset \Gamma^+), \end{cases} \tag{9}$$

$$\vec{T} = \begin{cases} A_p^I \vec{\bar{T}}_p^I \, \mathrm{e}^{\mathrm{i}k_p x_1} + \sum\limits_n A_n^- \vec{\bar{T}}_n^- \, \mathrm{e}^{-\mathrm{i}k_n x_1} & (x_1 \subset \Gamma^-), \\ \sum\limits_n A_n^+ \vec{\bar{T}}_n^+ \, \mathrm{e}^{\mathrm{i}k_n x_1} & (x_1 \subset \Gamma^+), \end{cases} \tag{10}$$

where subscripts n and p refer to nth or pth Lamb mode, A_p^I is the amplitude of the incident mode p, A_n^- and A_n^+ are the amplitudes of nth Lamb mode at edges Γ^- and Γ^+, respectively, k denotes the wavenumber, and $\vec{\bar{u}}^I$ (or $\vec{\bar{T}}^I$), $\vec{\bar{u}}^-$ (or $\vec{\bar{T}}^-$) and $\vec{\bar{u}}^+$ (or $\vec{\bar{T}}^+$) are the displacement (or stress) mode shape of the incident, left and right propagating waves, respectively. The Lamb mode shapes are given as [12]

For symmetric Lamb modes:

$$\vec{\bar{u}} = \begin{Bmatrix} \bar{u}_1 \\ \bar{u}_2 \end{Bmatrix} = \begin{Bmatrix} \mathrm{i}k \cos \alpha x_2 + \mathrm{i}C\beta \cos \beta x_2 \\ -\alpha \sin \alpha x_2 + Ck \sin \beta x_2 \end{Bmatrix}, \tag{11a}$$

$$\vec{\bar{T}} = \begin{Bmatrix} \bar{T}_{11} \\ \bar{T}_{12} \end{Bmatrix} = \begin{Bmatrix} \mu\{[2\alpha^2 - \xi^2(k^2+\alpha^2)] \cos \alpha x_2 - 2k\beta C \cos \beta x_2\} \\ \mathrm{i}\mu[-2\alpha k \sin \alpha x_2 - (\beta^2 - k^2)C \sin \beta x_2] \end{Bmatrix}; \tag{11b}$$

For anti-symmetric Lamb modes:

$$\vec{\bar{u}} = \begin{Bmatrix} \bar{u}_1 \\ \bar{u}_2 \end{Bmatrix} = \begin{Bmatrix} \mathrm{i}k \sin \alpha x_2 - \mathrm{i}D\beta \sin \beta x_2 \\ -\alpha \cos \alpha x_2 + Dk \cos \beta x_2 \end{Bmatrix}, \tag{11c}$$

$$\vec{\bar{T}} = \begin{Bmatrix} \bar{T}_{11} \\ \bar{T}_{12} \end{Bmatrix} = \begin{Bmatrix} \mu\{[2\alpha^2 - \xi^2(k^2+\alpha^2)] \sin \alpha x_2 + 2k\beta C \sin \beta x_2\} \\ \mathrm{i}\mu[2\alpha k \cos \alpha x_2 - (\beta^2 - k^2)D \cos \beta x_2] \end{Bmatrix}, \tag{11d}$$

where μ is the shear modulus, $\xi = C_p/C_s$, $\alpha^2 = \omega^2/C_p^2 - k^2$, $\beta^2 = \omega^2/C_s^2 - k^2$,

$$C = \frac{2k\alpha \sin(\alpha h/2)}{(k^2-\beta^2)\sin(\beta h/2)} \quad \text{and} \quad D = \frac{-2k\alpha \cos(\alpha h/2)}{(k^2-\beta^2)\cos(\beta h/2)}.$$

If each edge is discretized into l nodes and if N modes of Lamb waves are considered, Eqs. (9) and (10) can be expressed as [9]

$$\{\vec{u}\}^{\Gamma^-}_{l\times 1} = [\vec{\bar{u}}]^I_{l\times N}\{A^I_p\delta_{pn}\,\mathrm{e}^{\mathrm{i}k_n x_1}\}_{N\times 1} + [\vec{\bar{u}}]^-_{l\times N}\{A^-_n\mathrm{e}^{-\mathrm{i}k_n x_1}\}_{N\times 1}, \tag{12}$$

$$\{\vec{T}\}^{\Gamma^-}_{l\times 1} = [\vec{\bar{T}}]^I_{l\times N}\{A^I_p\delta_{pn}\,\mathrm{e}^{\mathrm{i}k_n x_1}\}_{N\times 1} + [\vec{\bar{T}}]^-_{l\times N}\{A^-_n\,\mathrm{e}^{-\mathrm{i}k_n x_1}\}_{N\times 1} \tag{13}$$

for the left edge, and

$$\{\vec{u}\}^{\Gamma^+}_{l\times 1} = [\vec{\bar{u}}]^+_{l\times N}\{A^+_n\,\mathrm{e}^{\mathrm{i}k_n x_1}\}_{N\times 1}, \tag{14}$$

$$\{\vec{T}\}^{\Gamma^+}_{l\times 1} = [\vec{\bar{T}}]^+_{l\times N}\{A^+_n\,\mathrm{e}^{\mathrm{i}k_n x_1}\}_{N\times 1} \tag{15}$$

for the right edge.

From Eq. (12), the amplitudes of the left propagating modes can be expressed as

$$\{A^-_n\mathrm{e}^{-\mathrm{i}k_n x_1}\}_{N\times 1} = [\vec{\bar{u}}^{-1}]^-_{N\times l}\{\vec{u}\}^-_{l\times 1} - [\vec{\bar{u}}^{-1}]^-_{N\times l}[\vec{\bar{u}}]^I_{l\times N}\{A^I_p\delta_{pn}\mathrm{e}^{\mathrm{i}k_n x_1}\}_{N\times 1}. \tag{16}$$

Substituting Eq. (16) into Eq. (13), the stress field at the left edge can be written in terms of the displacement field as

$$\{\vec{\bar{T}}\}^{\Gamma^-}_{l\times 1} = ([\vec{\bar{T}}]^I_{l\times N} - [\vec{\bar{T}}]^-_{l\times N}[\vec{\bar{u}}^{-1}]^-_{N\times l}[\vec{\bar{u}}]^I_{l\times N})\{A^I_p\delta_{pn}\mathrm{e}^{\mathrm{i}k_n x_1}\}_{N\times 1} + [\vec{\bar{T}}]^-_{l\times N}[\vec{\bar{u}}^{-1}]^-_{N\times l}\{\vec{u}\}^-_{l\times 1}. \tag{17}$$

Similarly, from Eqs. (14) and (15), the stress field at the right edge can be expressed as

$$\{\vec{\bar{T}}\}^{\Gamma^+}_{l\times 1} = [\vec{\bar{T}}]^+_{l\times N}[\vec{\bar{u}}^{-1}]^+_{l\times N}\{\vec{u}\}^+_{l\times 1}. \tag{18}$$

Considering a plate segment with traction-free boundaries and imaginary edges (Fig. 1), Eq. (8) can be equivalently expressed as

$$[H^{\mathrm{Top}}, H^{\mathrm{Bot}}, H^{\Gamma^-}, H^{\Gamma^+}][\vec{u}^{\mathrm{Top}}, \vec{u}^{\mathrm{Bot}}, \vec{u}^{\Gamma^-}, \vec{u}^{\Gamma^+}]' = [G^{\mathrm{Top}}, G^{\mathrm{Bot}}, G^{\Gamma^-}, G^{\Gamma^+}][0, 0, \vec{T}^{\Gamma^-}, \vec{T}^{\Gamma^+}]', \tag{19}$$

where each matrix is divided into four sub-matrices according to top, bottom, left and right boundaries, respectively, and the prime ($'$) denotes matrix transpose. Substituting Eqs. (17) and (18) into Eq. (19) and moving the unknown displacement fields from the right- to the left-hand side,

$$[H^{\mathrm{Top}}, H^{\mathrm{Bot}}, \bar{H}^{\Gamma^-}, \bar{H}^{\Gamma^+}][\vec{u}^{\mathrm{Top}}, \vec{u}^{\mathrm{Bot}}, \vec{u}^{\Gamma^-}, \vec{u}^{\Gamma^+}]' = B, \tag{20}$$

where

$$\bar{H}^{\Gamma^-} = H^{\Gamma^-} - G^{\Gamma^-}([\vec{\bar{T}}]^-_{l\times N}[\vec{\bar{u}}^{-1}]^-_{N\times l}), \tag{21}$$

$$\bar{H}^{\Gamma^+} = H^{\Gamma^+} - G^{\Gamma^+}([\vec{\bar{T}}]^+_{l\times N}[\vec{\bar{u}}^{-1}]^+_{N\times l}) \tag{22}$$

and

$$B = G^{\Gamma^-}(([\vec{\bar{T}}]^I_{l\times N} - [\vec{\bar{T}}]^-_{l\times N}[\vec{\bar{u}}^{-1}]^-_{N\times l}[\vec{\bar{u}}]^I_{l\times N})\{A^I_p\delta_{pn}e^{ik_nx_1}\}_{N\times 1}). \tag{23}$$

After solving Eq. (20), the amplitudes of the reflected and transmitted wave modes can be obtained as

$$\{A^-_n\, e^{-ik_nx_1}\}_{N\times 1} = [\vec{\bar{u}}^{-1}]^-_{N\times l}(\{\vec{u}\}^{\Gamma^-}_{l\times 1} - [\vec{\bar{u}}]^I_{l\times N}\{A^I_p\delta_{pn}e^{ik_nx_1}\}_{N\times 1}), \tag{24}$$

$$\{A^+_n e^{ik_nx_1}\}_{N\times 1} = [\vec{\bar{u}}^{-1}]^+_{N\times l}\{\vec{u}\}^{\Gamma^+}_{l\times 1}. \tag{25}$$

Normalizing by the amplitude of the incident wave gives the reflection and transmission coefficients.

In summary, the BEM presented by Cho and Rose [9] monitors the imaginary edge by linking the displacement and stress field through mode expansion [14], and hence provides a convenient way to study localized Lamb wave propagation and interaction characteristics without considering the reflections from the actual left and right edges of the plate boundary. Both imaginary left and right edges are discretized into small elements and the displacement and stress relationships are imposed on each node, resulting in the terms $\bar{H}^{\Gamma^-}$ and $\bar{H}^{\Gamma^+}$, thus forming a system of algebraic equations (20). Higher-order elements can be used to compute the terms, H^{Γ^-}, G^{Γ^-} H^{Γ^+} and G^{Γ^+} to achieve better accuracy and faster convergence in general for BEM programs. However, in the BEM formulated by forcing the wave mode shapes, these terms contain nonlinear mode shapes at each discrete node in Eqs. (21) and (22). Therefore, Cho and Rose [9] claimed that using a higher-order element cannot provide better solution, and all of their computations are based on linear element only. The consequence is that the imaginary edges have to be discretized into very fine elements and computational efficiency is therefore reduced.

2.3. Wave element in BEM for Lamb wave problems

To overcome this limitation, a wave element is proposed in this paper. Since Lamb wave mode shapes describe very closely the exact shapes of displacements and stresses on the edges, they are therefore almost optimal for use as interpolating function of the element. By formulating an element that can describe almost the exact shapes, it is no longer necessary to subdivide each edge. A single element spans the entire edge and is termed herein as the wave boundary element (WBE). By separating the edges from other boundaries, Eq. (1) can be written as

$$c^i\vec{u}^i + \int_{\Gamma^{\mathrm{Top}}+\Gamma^{\mathrm{Bot}}} \vec{T}^*\,\vec{u}\,d\Gamma + \int_{\Gamma^-+\Gamma^+} \vec{T}^*\,\vec{u}\,d\Gamma = \int_{\Gamma^{\mathrm{Top}}+\Gamma^{\mathrm{Bot}}} \vec{u}^*\,\vec{T}\,d\Gamma + \int_{\Gamma^-+\Gamma^+} \vec{u}^*\,\vec{T}\,d\Gamma. \tag{26}$$

Substituting Eqs. (9) and (10) into Eq. (26) and grouping terms with common unknown variables A_n^- and A_n^+ give

$$c^i\vec{u}^i + \int_{\Gamma^{\mathrm{Top}}+\Gamma^{\mathrm{Bot}}} \vec{T}^*\,\vec{u}\,\mathrm{d}\Gamma + \sum_n \left[\int_{\Gamma^-} (\vec{T}^*\,\vec{\bar{u}}_n^- - \vec{u}^*\,\vec{\bar{T}}_n^-)\mathrm{e}^{-\mathrm{i}k_n x_1}\,\mathrm{d}\Gamma\right] A_n^- + \sum_n \left[\int_{\Gamma^+} (\vec{T}^*\,\vec{\bar{u}}_n^+ - \vec{u}^*\,\vec{\bar{T}}_n^+)\mathrm{e}^{\mathrm{i}k_n x_1}\,\mathrm{d}\Gamma\right] A_n^+ = \int_{\Gamma^{\mathrm{Top}}+\Gamma^{\mathrm{Bot}}} \vec{u}^*\,\vec{T}\,\mathrm{d}\Gamma - \left[\int_{\Gamma^-} (\vec{T}^*\,\vec{\bar{u}}_p^I - \vec{u}^*\,\vec{\bar{T}}_p^I)\mathrm{e}^{\mathrm{i}k_p x_1}\,\mathrm{d}\Gamma\right] A_p^I. \tag{27}$$

By discretizing the top and bottom boundaries only, Eq. (27) can be expressed as

$$c^i\vec{u}^i + [\hat{H}^{\mathrm{Top}}, \hat{H}^{\mathrm{Bot}}][\vec{u}^{\mathrm{Top}}, \vec{u}^{\mathrm{Bot}}]' + \sum_n \bar{H}_n^{\Gamma^-} A_n^- + \sum_n \bar{H}_n^{\Gamma^+} A_n^+ = [G^{\mathrm{Top}}, G^{\mathrm{Bot}}][\vec{T}^{\mathrm{Top}}, \vec{T}^{\mathrm{Bot}}]' - \bar{H}_p^I A_p^I, \tag{28}$$

where

$$\bar{H}_n^{\Gamma^-} = \int_{\Gamma^-} (\vec{T}^*\vec{\bar{u}}_n^i - \vec{u}^*\vec{\bar{T}}_n^-)\mathrm{e}^{-\mathrm{i}k_n x_1}\,\mathrm{d}\Gamma, \tag{29}$$

$$\bar{H}_n^{\Gamma^+} = \int_{\Gamma^+} (\vec{T}^*\vec{\bar{u}}_n^+ - \vec{u}^*\vec{\bar{T}}_n^+)\mathrm{e}^{\mathrm{i}k_n x_1}\,\mathrm{d}\Gamma, \tag{30}$$

$$\bar{H}_p^I = \int_{\Gamma^-} (\vec{T}^*\vec{\bar{u}}_p^I - \vec{u}^*\vec{\bar{T}}_p^I)\mathrm{e}^{\mathrm{i}k_p x_1}\,\mathrm{d}\Gamma. \tag{31}$$

The integrals in Eqs. (29)–(31) are integrated numerically without subdivision, considering both fundamental solutions $\vec{T}^*$ and $\vec{u}^*$, and mode shapes $\vec{\bar{T}}$ and $\vec{\bar{u}}$. The unknowns on the edges are now the amplitudes of each mode, and the degree of freedom for each edge is only the number of modes that are present.

If Γ^{Top} and Γ^{Bot} are discretized into a total of L nodes, a system of $2L$ equations can be formed by applying Eq. (28) at each node i in the direction x_1 and x_2, one at a time. The system of equations has $2L + 2J$ unknowns to be determined, where J is the number of Lamb modes considered at each edge. Therefore, additional J nodal points are required at the edges to form $2J$ equations through Eq. (28).

Examining the fundamental solutions $\vec{T}^*$ and $\vec{u}^*$, Eqs. (29)–(31) become singular when the collecting point lies on the wave element that is being integrated. This, however, can be overcome by examining Eq. (28) in detail. Consider the case where the collecting point is located in edge Γ^+. The singularity occurs only in terms involving integration in the domain Γ^+, namely Eq. (30).

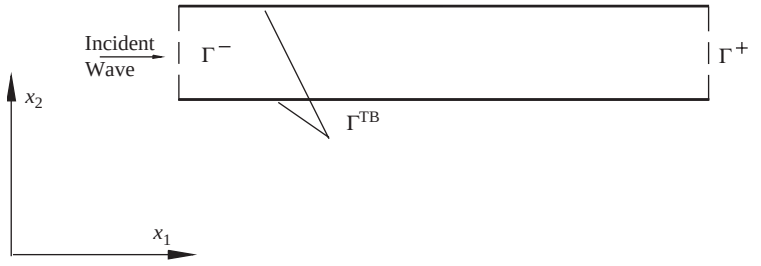

Fig. 2. Uniform plate segment.

Re-grouping the terms in Eq. (28) yields

$$[\hat{H}^{\mathrm{Top}}, \hat{H}^{\mathrm{Bot}}][\vec{u}^{\mathrm{Top}}, \vec{u}^{\mathrm{Bot}}]' + \sum_n \bar{H}_n^{\Gamma^-} A_n^- + \sum_n (\bar{H}_n^{\Gamma^+} + c^i \vec{\bar{u}}_n^i) A_n^+ = [G^{\mathrm{Top}}, G^{\mathrm{Bot}}][\vec{T}^{\mathrm{Top}}, \vec{T}^{\mathrm{Bot}}]' - \bar{H}_p^I A_p^I. \tag{32}$$

It should be noted that, mathematically, $\bar{H}_n^{\Gamma^+} + c^i \vec{\bar{u}}_n^i$ depends only on Γ^+ and does not involve other boundaries. This term can therefore be evaluated using a similar plate with simpler geometry as long as Γ^+ remains unchanged, such as the plate in Fig. 2, where the other three boundaries are a similar imaginary left edge Γ_g^- and plane traction-free surfaces Γ_g^{TB} without any structural discontinuity, in which subscript g is used to reference the fictitious plate. For Lamb mode n propagating out of the plate from the edge Γ_g^- with an amplitude of A_n^+, there must be a same Lamb mode n propagating into the segment from Γ^+ with amplitude A_n^+ and the wave field on Γ_g^{TB} must correspond to the same Lamb mode of amplitude A_n^+ because there is no any structural discontinuity to cause wave decay, reflection, scattering or mode conversion. Therefore, applying Eq. (28) to the fictitious segment gives

$$\sum_n \hat{H}_g^{\mathrm{TB}} \vec{\bar{u}}_n^{\mathrm{TB}} A_n^+ + \sum_n \bar{H}_n^{\Gamma_g^-} A_n^+ \sum_n (\bar{H}_n^{\Gamma^+} + c^i \vec{\bar{u}}_n^i) A_n^+ = [G_g^{\mathrm{TB}}][0]. \tag{33}$$

The variables A_n^+ can be factored out and hence the singular term can be obtained as

$$(\bar{H}_n^{\Gamma^+} + c^i \vec{\bar{u}}_n^i) = -\hat{H}_g^{\mathrm{TB}} \vec{\bar{u}}_n^{\mathrm{TB}} - \bar{H}_n^{\Gamma_g^-}. \tag{34}$$

In summary, this method treats each imaginary edge as a WBE, thus significantly reducing the degree of freedom associated with the edges. Since the shape functions used are exact solutions of Lamb modes, the accuracy is predominantly controlled by the numerical integration scheme, namely Gauss quadrature. Hence, using WBE with the proposed method to overcome the singularity facilitates better accuracy and computational efficiency simultaneously.

2.4. Accuracy and efficiency of the proposed method

A uniform plate segment without any discontinuity (Fig. 2) is computed using both the hybrid BEM proposed by Cho and Rose [9] and the wave element method to compare their accuracy and computational efficiency.

A 2 mm thick and 16 mm long uniform segment was used to calculate the amplitudes of Lamb modes propagating out from the two imaginary edges when unit amplitude of one specific Lamb mode is incident to the segment from the left edge. The actuation frequency considered is 600 kHz, which can be employed for actual NDE on 2 mm aluminum plates [4,5]. Only the lowest two Lamb modes exist at this frequency range, namely, the fundamental anti-symmetric mode A_0 with wavelength 4 mm, and symmetric mode S_0 with wavelength 8.7 mm. Quadratic element of length 0.4 mm (distance between nodes is 0.2 mm) is used to discretize the top and bottom surfaces. Hence, the total number of nodes on both surfaces are $L = 2 \times 16/0.2 = 160$.

The edges when modeled using WBE need not be discretized. Since only two modes exists, $J = 2$, only 2 nodes from the edges together with L nodes from surfaces are used as collecting point to form a $(2L + 2J) \times (2L + 2J) = 324 \times 324$ system of equation by applying Eq. (28) $2L + 2J$ times. When an A_0 wave of unit amplitude propagates into the segment, that is, the input $A_p^I = A_{A_0}^I = 1$ in Eq. (28), the solutions for the amplitudes of the reflected and transmitted modes are $[A_{A_0}^-, A_{S_0}^-, A_{A_0}^+, A_{S_0}^+] =$ [0.018, 0.000, 0.985, 0.000], where the subscript is used to denote the particular mode. It should be noted that $A_{A_0}^+ = 0.985$ represents 100% transmission, with 1.5% error, $A_{A_0}^- = 0.018$ represents 0% reflection with 1.8% error, $A_{S_0}^- = 0.000$ and $A_{S_0}^+ = 0.000$ imply the absence of S_0 wave meaning that no mode conversion occurs. The results agree with the physical fact that without structural discontinuity in the segment, the input wave mode propagates to the right edge without any decay, reflection, or mode conversion. The displacement fields at the surfaces of the segment are visualized in Fig. 3, with amplitudes normalized by their maximum values, respectively. The wavelength estimated from Fig. 3a or b is approximately

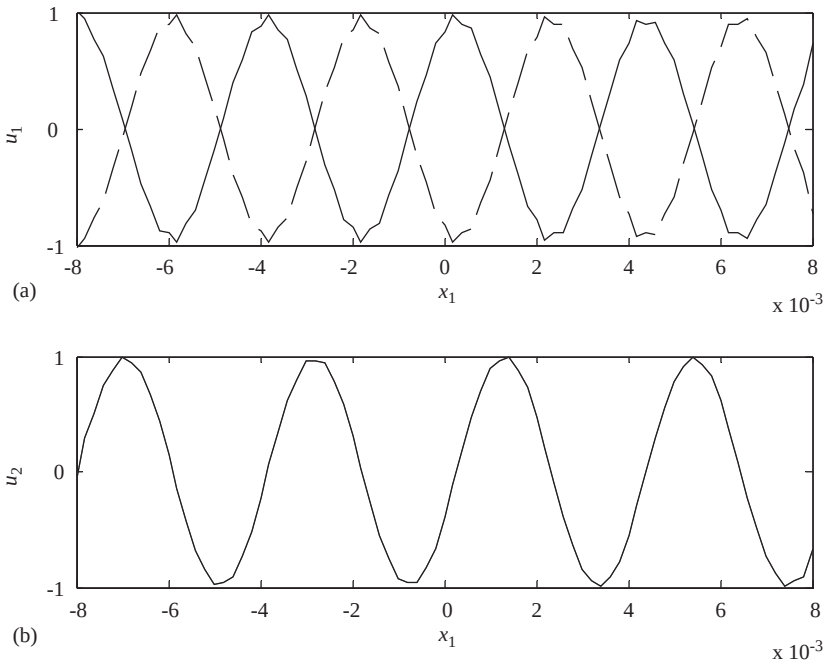

Fig. 3. Displacement field on plate surfaces; (a) solid line for bottom surface and dashed line for top surface (both lines are coincident in (b)).

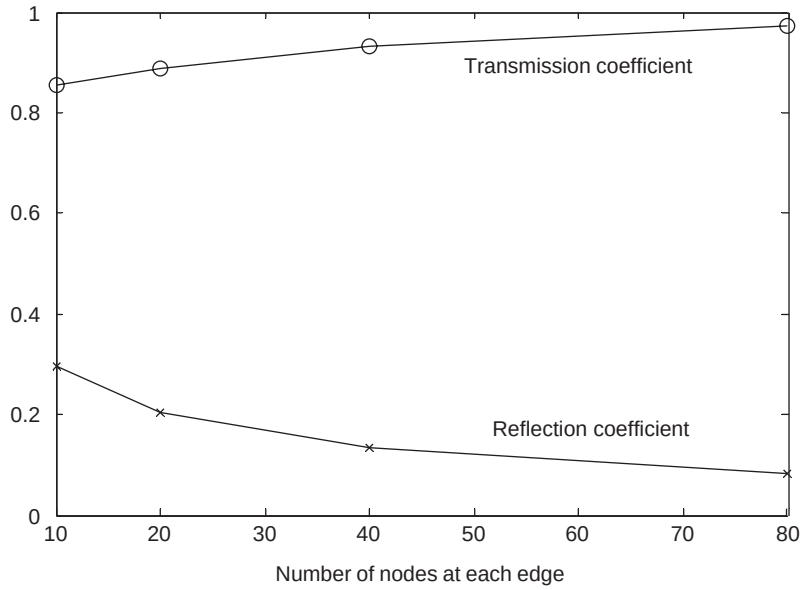

Fig. 4. Convergence of hybrid BEM with respect to edge discretization.

4 mm, matching the wavelength of A_0. Displacement in longitudinal direction, u_1 (in Fig. 3a), is anti-symmetric, while displacement in transversal direction, u_2 (in Fig. 3b), is symmetric (two lines for top and bottom surface coincident). This produces a resultant almost circular particle motion in the clockwise direction at the top surface and anti-clockwise direction at the bottom surface, consistent with the motion of anti-symmetric wave mode.

The results above are obtained by treating each imaginary edge as a whole WBE. Comparison study has been performed by discretizing each imaginary edge into 2 WBE, and three nodal points from each edge are used as collecting points to form the equations. The over-determined system of equations is then solved using the method of least squares. The result shows no improvement in accuracy indicating the convergence and adequacy of using only one WBE for each edge and the appropriateness of the mode shape function in representing the wave field distribution.

The left and right edges of the same plate are discretized into elements ranging from 10 to 80 and solutions computed using the method of Cho and Rose [9] for comparison purpose. The convergence with respect to the degree of discretization is plotted in Fig. 4. It is noted that the same accuracy as in the modified method can be achieved only after at least a total of $L' = 2 \times 80$ nodes are used for two edges. This results in a system of equation of size $(2L + 2L') \times (2L + 2L') = 640 \times 640$. Hence, more terms need to be formulated since the matrix has $(2L + 2L') \times (2L + 2L')/[(2L + 2J) \times (2L + 2J)] \approx 4$ times the number of entries compared to that of the proposed method.

3. Modeling of Lamb wave interaction with notches

For the plate shown in Fig. 1, incident wave from one edge will propagate and then interact with the notch, undergoing mode conversion. Hence, there will be reflected waves traveling

towards the left edge and transmitted waves towards to the right edge. If the incident wave is fixed, the reflection and transmission coefficients are affected by the severity of the structural discontinuity, which in this case is the notch geometry. These coefficients measured experimentally in NDT can be used as a quantitative means to characterize the discontinuity and confirmed by computational means. To facilitate comparison with experimental results from the previous NDE work [4], all the computations are performed using 600 kHz wave on 2 mm aluminum plates.

A program has been written to mesh the boundaries of the plate segment including the notch. Each linear surface of the notch is discretized into 10 quadratic elements. To analyze the sensitivity of the Lamb waves to the size of the notch, the reflection coefficients of A_0 and S_0 from the notch are computed using BEM for notch depth varying from 0.2 to 1.8 mm at a fixed notch width of 1 mm. The results are shown in Fig. 5 for A_0 input and Fig. 6 for S_0 input. The reflection coefficients of A_0 and S_0 from a notch have been studied by Lowe et al. [15] and by Lowe and Diligent [16] by using an in-house FEM software. The results in Figs. 5a and 6b agree with their results. The variation of reflection coefficient against notch depth has been discussed using quasi-static assumption when the wavelength is much larger than the notch size, and using ray theory when the wavelength is much smaller. In the practical situation, where notch size is of the same order of the wavelength, the results vary between the values from these two theories. A simpler interpretation of the reflection coefficient curves against notch depth can be made here based on Figs. 5 and 6 by considering mode shape and energy conservation with respect to transmission, reflection, and mode conversion.

The case of A_0 input is first discussed based on Fig. 5. The notch depth is normalized by the plate thickness, $\bar{d} = d/h$. As shown in Fig. 5a, for $\bar{d} < 0.3$, the notch depth is less than 1/7 the

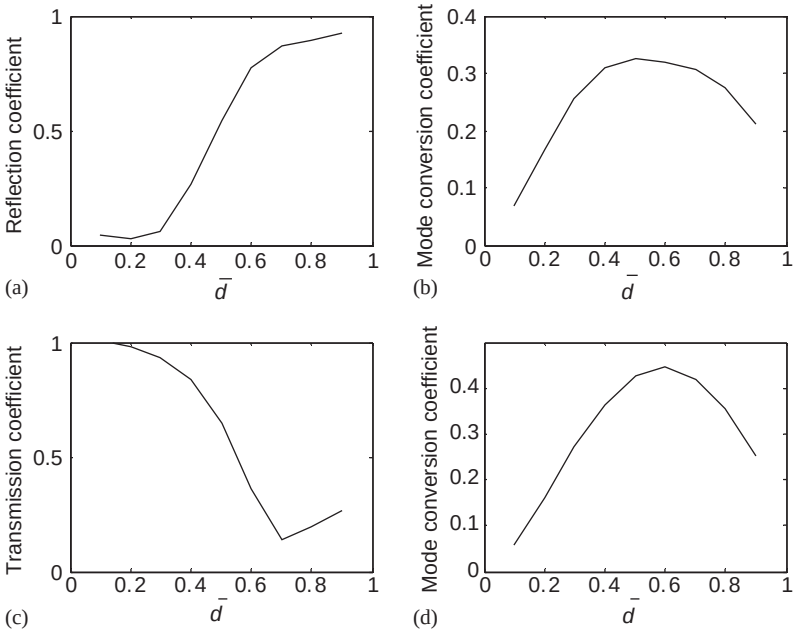

Fig. 5. Coefficients against normalized notch depth for A_0 input. (a) Reflected A_0, (b) reflected S_0, (c) transmitted A_0 and (d) transmitted S_0.

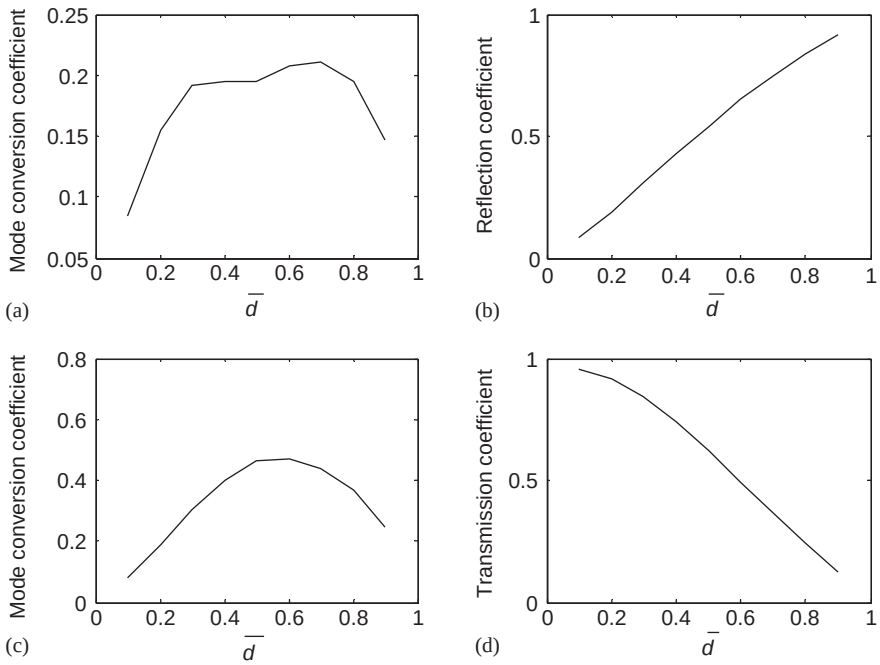

Fig. 6. Coefficients against normalized notch depth for S_0 input. (a) Reflected A_0, (b) reflected S_0, (c) transmitted A_0 and (d) transmitted S_0.

wavelength of A_0 (where the latter is 4 mm). Hence, the wave will transmit through the notch almost completely with negligible reflection, which agrees well with the low coefficients obtained for both the reflected A_0 and S_0 wave components. If the notch spans over the full depth, then the A_0 wave is fully reflected with no conversion. The coefficient for the reflected A_0 wave component approaches 1 and that for the reflected S_0 wave approaches 0. In between these two extremes, the incident A_0 wave will undergo mode conversion, partially transmitted and partially reflected containing both A_0 and S_0 components. For surface cracks deeper than 1/7 wavelength, the reflection coefficients of A_0 wave may be used to characterize the presence of a notch as it increases with notch depth. It is also not surprising that in Fig. 5b and d, the reflected and transmitted S_0 coefficient first increases and then decreases with depth, with the maximum value occurring when the notch depth is close to half the thickness of the plate. The curve in Fig. 5c has a slight upward tail because the mode conversion drops too rapidly as the notch depth increases that conversion may not be complete. The unconverted energy remains in the transmitted A_0 wave, resulting in a slight increase even though the notch depth increases.

The coefficients of S_0 input are plotted in Fig. 6. A similar phenomenon can be observed where mode conversion is maximum when notch depth is about half through the plate thickness (Fig. 6a and c). Unlike A_0, S_0 exhibits good sensitivity even for a shallow notch. For $\bar{d} = 0.2$, the notch depth around 1/20 wavelength of S_0 (where the latter is 8.7 mm) and the reflection can be distinctly observed. This could be due to its small value at the surface that any change becomes significant. The existence of surface crack destroys the symmetry of the wave, resulting in mode

conversion. It is shown here that the mode shape also contributes significantly to the sensitivity of the detection. This is consistent with the observation by Ditri et al. [17] that energy distribution inside a plate for different Lamb modes could be used to predict their detectability due to the presence of cracks.

Similar analysis can be performed to evaluate the dependence of the coefficients on notch width, which for concise reasons will not be discussed in detail. They agree well with the results presented by Lowe et al. [15], and Lowe and Diligent [16]. The variation of the coefficients exhibited against notch width is somewhat periodic and relates to the wavenumbers of the Lamb modes.

4. Time domain analysis

The proposed method is formulated in the frequency domain. The solution obtained corresponds to the coefficients for a specific frequency in a steady-state elasto-dynamics problem. In wave pulse generation for NDE of plates, the incident wave package is described in time domain, denoted as $f(t)$, and can be digitized into $f(j)$ for each discrete time instance t_j, where $j = 1, 2, \ldots, m$. Fast Fourier transform algorithm can then be employed to perform discrete Fourier transform to convert the temporal signals into frequency domain as $F(p)$,

$$F(p) = \sum_{j=1}^{m} f(j)\omega_m^{(j-1)(p-1)}, \tag{35}$$

where $\omega_m = e^{(-2\pi i)/m}$ is the mth root of unity and $j = 1, 2, \ldots, m$.

For each specific frequency ω_p, the coefficients $A_n(p)$ can be calculated in the frequency domain using the method presented earlier, where n denotes Lamb mode n. By using inverse Fourier transform, response time history for each Lamb mode is obtained as pulse packages, that is

$$\bar{f}_n(j) = \frac{1}{m}\sum_{p=1}^{m} A_n(p)\omega_m^{-(j-1)(p-1)}. \tag{36}$$

If the incidence is narrow banded in frequency, for example, a package of double-exponential windowed sinusoidal waves (Fig. 7a), $F(p)$ only has significant value concentrated at the vicinity of the central frequency, while the energy distributed away from the central frequency is negligible (see Fig. 7b). By taking only the significant value, the frequency function $F(p)$ can be reconstructed as

$$F'(p) = \begin{cases} F(p), & \text{abs}(F(p)) \geqslant g, \\ 0, & \text{abs}(F(p)) < g, \end{cases} \tag{37}$$

where abs() takes the absolute value of the variable inside the brackets, and $0 < g < 1$ is a threshold value to be specified to meet accuracy requirements. It is found in this study that $g = 0.2$ is sufficient to give fairly accurate reconstructed time history response from the approximated frequency function (see Fig. 7c). Therefore, the calculation is performed $p_2 - p_1 + 1$ times only to obtain the coefficients $A_n(p)$ for each discrete frequency within $\omega_{p_1} - \omega_{p_2}$, where p_1 and p_2 are obtained from $\text{abs}(F(p)) \geqslant g$. The value of $A_n(p)$, $p < p_1$ or $p > p_2$, are padded with zero to construct $A_n(p)$ into an array with m elements to be substituted into Eq. (36).

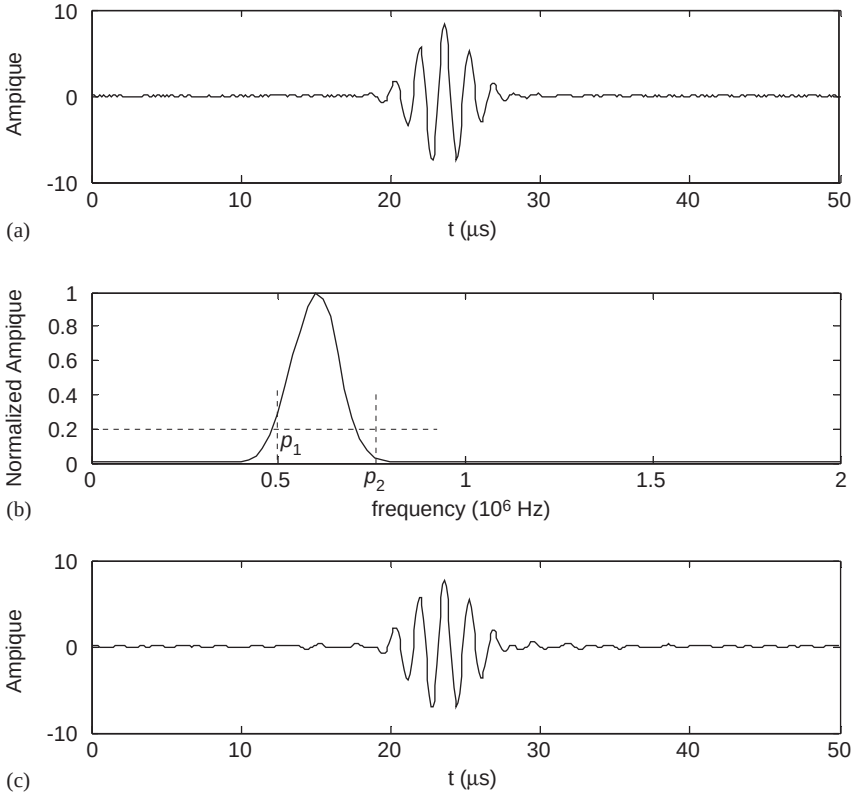

Fig. 7. (a) The incidence of exponential windowed sine cycles in time history; (b) Fourier transformed incident signal in frequency domain; and (c) time history signals by inverse Fourier transform from reconstructed frequency function of threshold value $g = 0.2$.

Each Lamb package propagates at its group wave velocity, v_g^n, which can be calculated numerically via $v_g^n = \mathrm{d}\omega/\mathrm{d}k_n$, where k_n is the wavenumber of Lamb mode n [12]. Without loss of generality, assuming only the two fundamental modes A_0 and S_0 exist and the input is an A_0 pulse, the wave package propagates from the left imaginary edge to the structural discontinuity at group velocity $v_g^{A_0}$. Due to interaction with the discontinuity, a part of the incident energy reflects as A_0 wave propagating at $v_g^{A_0}$ to the left imaginary edge, and a part of the incidence energy converts into S_0 wave, propagating at $v_g^{S_0}$ to the left imaginary edge. The remaining energy of the incident wave transmits through the discontinuity and propagates to the right imaginary edge partially as A_0 wave at $v_g^{A_0}$ and partially as S_0 wave at $v_g^{S_0}$. Therefore, for A_0 incidence, there are two packages expected at the left imaginary edge, denoted as A_0–A_0 and A_0–S_0, respectively. The lag time for them to propagate from the left edge to the discontinuity and reflect back to the left edge can be calculated as $t_{A-A} = 2L_c/v_g^{A_0}$ and $t_{A-S} = L_c/v_g^{A_0} + L_c/v_g^{S_0}$, respectively, where L_c is the distance from the left imaginary edge to the discontinuity. By shifting the time response for each mode obtained from Eq. (36) with its respective lag time and superimposing all the reflected modes, the time history at the left imaginary edge can be constructed. Similarly, the time history at

the right imaginary edge can be constructed as well by superimposing all the transmitted modes shifted with their respective lag time.

5. Experiments

NDE experiments were performed for 2 mm aluminum plates [4]. The numerical results using BEM help explain some experimental results that seem at first to be incorrect. First, in detecting a 0.7 mm deep notch in a 2 mm aluminum plate by generating A_0 wave at 600 kHz, the reflected wave contained both A_0 and S_0 components as a result of mode conversion (Fig. 5b). When detecting a 1.8 mm deep notch under the same experimental condition, the reflected A_0 wave was strong but the reflected S_0 wave was missing. This appears incorrect as one would expect to detect some S_0 component. The experimental result that mode conversion decreases rapidly when the notch depth increases from half-thickness to a through crack is, however, confirmed numerically by Fig. 5b.

Experiments were also carried out to test the sensitivity of A_0 and S_0 waves for a shallow notch. A 0.5 mm deep, 1 mm wide notch was cut on a $600 \times 600 \times 2$ mm aluminum plate for this purpose. S_0 and A_0 waves were generated by imposing a 5-cycle 600 kHz windowed electrical pulse (Fig. 7a) from a function generator to a wideband circular piezoceramic actuator (8 mm diameter by 0.5 mm thick), and a similar piezoceramic sensor to collect the Lamb wave signals to a digital oscilloscope as illustrated in Fig. 8. The output signal read by the oscilloscope is shown in Fig. 9. By using their flight time and the group velocities of S_0 and A_0 (S_0 is faster than A_0), the collected signal packages can be identified from left to right, annotated in the figure as associated with the excitation signal, S_0 (direct incident S_0 wave), A_0 (direct incident A_0 wave), A_0' ('ringing' signal of incident A_0 wave due to circular piezoelectric patch used), S_0–S_0 (S_0 wave reflected by notch from incident S_0 wave), S_0–A_0 (A_0 wave mode converted and reflected by notch from incident S_0 wave), A_0–S_0 (S_0 wave mode converted and reflected by notch from incident A_0 wave), A_0–A_0 (A_0 wave reflected by notch from incident A_0 wave) and reflection from the boundary.

The position of the sensor can be regarded as the reference left imaginary edge, and the incident Lamb modes S_0 and A_0 read from the digital oscilloscope can then be extracted from Fig. 9a as input for the numerical analysis and transformed into frequency domain using Eq. (35). The coefficients are computed at each discrete frequency component via Eq. (37) and the time history of each Lamb mode can then be obtained by Eq. (36). All the modes propagated to the left imaginary edge are superimposed accounting for their respective lag time. The computational results are given in Fig. 9b. By superimposing an expanded portion of Figs. 9a and b, and plotting in Fig. 9c, comparison can be made between the experimental (solid line) and computational (dotted line) results. Both the flight time and amplitudes of each package show good agreement.

It is noted that the amplitude of A_0–A_0 component is slightly smaller than that of S_0–S_0 component although the amplitude of the incident A_0 wave is larger than that of the incident S_0 wave. This is consistent with the earlier results of Figs. 5a and 6b, which indicates that S_0 wave is comparatively more sensitive to the shallow notch.

The presence of A_0' component can be explained by the fact that a simple circular piezoceramic patch is used, which cannot eliminate the 'ringing' phenomenon that is exhibited in the compliant

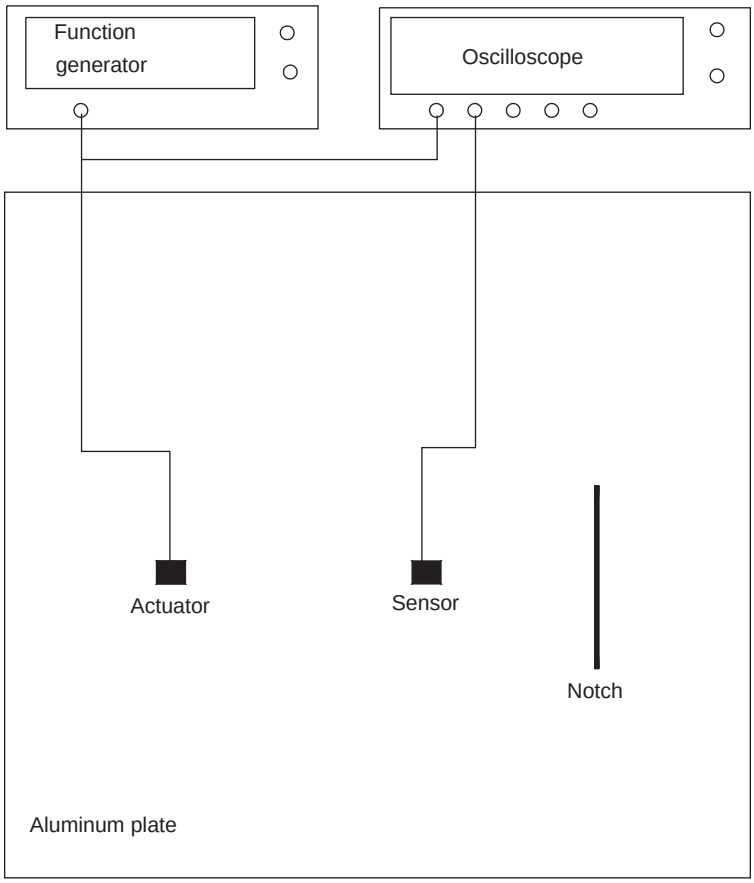

Fig. 8. Experimental set-up.

system. This undesirable ringing effect can be eliminated by using the improved excitation technique or actuator, such as the inter-digital transducer [4].

From numerical analysis and experimental results, quantitative NDE can be performed by measuring the coefficients of reflection and mode conversion. In general, the reflection increases with increase in notch depth. The depth of the notch is (i) shallow when both reflection and mode conversion coefficients are both low (in this case, reflection coefficient is lower than 0.1 and mode conversion coefficient is lower than 0.2), (ii) close to mid-depth when reflection coefficient is of intermediate value (from 0.2 to 0.8 in this case) and mode conversion coefficient is relatively high (above 0.25 in this case), and (iii) deep when the reflection coefficient is high (above 0.8 in this case) and mode conversion is low (lower than 0.25 in this case).

As illustrated in Fig. 9, generation of both A_0 and S_0 modes simultaneously makes it difficult to analyze the experimental data. Actually, the interpretation can be significantly simplified if a single mode is generated for NDE. Wave generation techniques, such as wedge transducers [1], comb transducers [2] and inter-digital transducers [3–5], can be employed to serve this purpose in practical NDE applications.

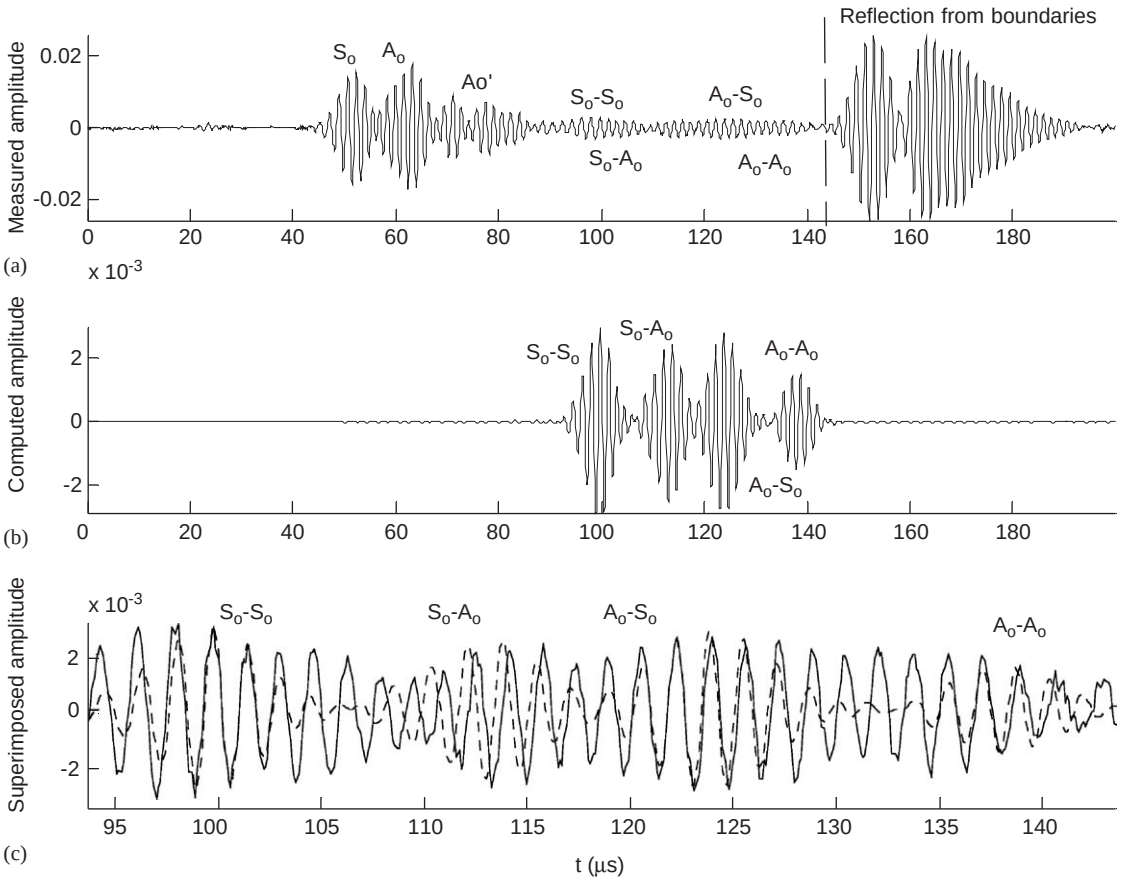

Fig. 9. Incident S_0 and A_0 waves on the plate with a shallow notch; (a) experimental readout from digital oscilloscope, (b) computational results and (c) expanded and superimposed experimental (solid line) with computational (dotted line) results.

6. Conclusion

A wave element is proposed in the boundary element method for the numerical study of Lamb wave propagation and interaction with structure discontinuity. It has the advantages of both accuracy and computational efficiency. Lamb wave interaction with a notch is investigated by using this method, and the results obtained are consistent with the physical consideration of Lamb mode shape and energy conservation with respect to transmission, reflection and mode conversion. Because of the symmetric mode shape, S_0 is more sensitive to the shallow notch than A_0. By making use of the fact that the reflection increases with increase in notch depth and mode conversion are maximized when the notch is around half through the thickness of the plate, the reflection and conversion coefficients can be used to characterize the depth of the notch. Numerical results obtained agree well with experimental results providing confidence to the BEM for the study of wave propagation in plates.

References

[1] X. Jia, B. Auld, G. Quentin, Normal-mode theory for analyzing the Lamb waves generation by a wedge transducer, *Proceedings of the 1995 World Congress on Ultrasonics*, 1995, pp. 317–321.
[2] J.L. Rose, S.P. Pelts, M.J. Quarry, A comb transducer model for guided wave NDE, *Ultrasonics* 36 (1998) 163–169.
[3] P. Wilcox, R. Monkhouse, M. Lowe, P. Cawley, The use of Huygens' principle to model the acoustic field from interdigital Lamb wave transducers, in: D. Thompson, D. Chimenti (Eds.), *Review of Progess in Quantitative Non-destructive Evaluation*, Vol. 1, Plenum Press, New York, 1998, pp. 915–922.
[4] J. Jin, Excitation and Propagation of Elastic Waves by Inter-digital Transducer for Nondestructive Evaluation of Plates, PhD Thesis, National University of Singapore, 2003.
[5] J. Jin, S.T. Quek, Q. Wang, Analytical solution of excitation of Lamb waves in plates by interdigital transducer, *Proceedings of the Royal Society of London, Series A* 2033 (2003) 1117–1134.
[6] Y.N. AI-Nassar, S.K. Datta, A.H. Shah, Scattering of Lamb waves by a normal rectangular strip weldment, *Ultrasonics* 29 (1991) 125–132.
[7] Z. Chang, Wave Propagation in a Plate with Defects, PhD Thesis, University of California, Los Angeles, 1997.
[8] E. Moulin, J. Assaad, C. Delebarre, Modeling of Lamb waves generated by integrated transducers in composite plates using a coupled finite element-normal modes expansion method, *Journal of the Acoustical Society of America* 107 (2000) 87–94.
[9] Y. Cho, J.L. Rose, A boundary element solution for a mode conversion study on the edge reflection of Lamb waves, *Journal of the Acoustical Society of America* 99 (1996) 2097–2109.
[10] Y. Cho, D.D. Hongerholt, J.L. Rose, Lamb wave scattering analysis for reflector characterization, *IEEE Transactions on Ultrasonics, Ferroelectrics and Frequency Control* 44 (1997) 44–52.
[11] X. Zhao, J.L. Rose, Boundary element modeling for defect characterization potential in a wave guide, *International Journal of Solids and Structures* 40 (2003) 2645–2658.
[12] K.F. Graff, *Wave Motion in Elastic Solids*, Oxford University Press, London, 1975.
[13] C.A. Brebbia, J. Dominguez, *Boundary Elements: An Introductory Course*, McGraw-Hill, New York, 1989.
[14] B.A. Auld, *Acoustic Fields and Waves in Solids*, Wiley, New York, 1973.
[15] M.J.S. Lowe, P. Cawley, J.-Y. Kao, O. Diligent, The low-frequency reflection characteristics of the fundamental antisymmetric Lamb wave A_0 Lamb wave from a rectangular notch in a plate, *Journal of the Acoustical Society of America* 112 (2002) 2612–2622.
[16] M.J.S. Lowe, O. Diligent, Low-frequency reflection characteristics of the S_0 Lamb wave from a rectangular notch in a plate, *Journal of the Acoustical Society of America* 111 (2002) 64–74.
[17] J.J. Ditri, J.L. Rose, G. Chen, Mode selection criteria for defect detection optimization using Lamb waves, in: D. Thompson, D. Chimenti (Eds.), *Review of Progress in Quantitative Non-destructive Evaluation*, Vol. 11, Plenum, New York, 1992, p. 2109.